Combined High Catalytic Activity and Efficient Polar Tubular Nanostructure in Urchin-like Metallic $NiCo_2Se_4$ for High Performance Lithium Sulfur Batteries

Chaoqi Zhang, Jordi Jacas Biendicho, Ting Zhang, Ruifeng Du, Junshan Li, Xuhui Yang, Jordi Arbiol, Yingtang Zhou,* Joan Ramon Morante, Andreu Cabot**

C. Q. Zhang, Dr. J. J. Biendicho, R. F. Du, J. S. Li, Prof. J. R. Morante, Prof. A. Cabot
Catalonia Institute for Energy Research - IREC
Sant Adrià de Besòs, Barcelona, 08930, Spain
Email: jjacas@irec.cat, andreucabot@gmail.com

C. Q. Zhang, R. F. Du, J. S. Li, Prof. J. R. Morante,
Departament of Physics
Universitat de Barcelona, 08028 Barcelona, Spain

T. Zhang, Prof. J. Arbiol
Catalan Institute of Nanoscience and Nanotechnology (ICN2)
CSIC and BIST, Campus UAB, Bellaterra, 08193 Barcelona, Spain

X. H. Yang
Key Laboratory of Eco-materials Advanced Technology, College of Materials Science and Engineering
Fuzhou University, Fuzhou 350108, P. R. China

Prof. J. Arbiol, Prof. A. Cabot
ICREA
Pg. Lluís Companys 23, 08010 Barcelona, Spain

Prof. Y. T. Zhou
Key Laboratory of Health Risk Factors for Seafood and Environment of Zhejiang Province, Institute of Innovation & Application
Zhejiang Ocean University, Zhoushan, Zhejiang Province, 316022, China
Email: zhouyingtang@zjou.edu.cn

Keywords: nickel cobalt selenide, catalytic effect, polarity, hollow nanostructure, lithium sulfur batteries

Abstract

Urchin shaped $NiCo_2Se_4$ (u-NCSe) nanostructures as efficient sulfur hosts are synthesized to overcome the limitations of lithium sulfur batteries (LSBs). u-NCSe provides a beneficial hollow structure to relieve volumetric expansion, a superior electrical conductivity to improve electron transfer, a high polarity to promote absorption of LiPS, and outstanding electrocatalytic activity to accelerate LiPS conversion kinetics. Owing to these excellent qualities as cathode for LSBs, S@u-NCSe delivers outstanding initial capacities up to 1403 mA h g^{-1} at 0.1 C, and retains 626 mAh g^{-1} at 5 C with exceptional rate performance. More significantly, a very low capacity decay rate of only 0.016% per cycle is obtained after 2000 cycles at 3 C. Even at high sulfur loading (3.2 mg cm^{-2}), a reversible capacity of 557 mA h g^{-1} is delivered after 600 cycles at 1 C. DFT calculations further confirm the strong interaction between NCSe and LiPS and cytotoxicity measurements prove the biocompatibility of NCSe. This work not only demonstrates that transition metal selenides can be promising candidates as sulfur host materials, but also provides a strategy for the rational design and the development of LSBs with long-life and high-rate electrochemical performance.

1. Introduction

The low energy density and relatively high price of traditional lithium-ion batteries (LIBs) are dramatically limiting their application in large-scale energy storage systems, especially in the fast-growing field of electric vehicles.[1,2] To overcome these two limitations, rechargeable lithium sulfur batteries (LSBs) have recently emerged as one of the most exciting alternatives to LIBs owing to their higher theoretical energy density (2600 W h kg^{-1}, 6 times higher than LIBs of 420 W h kg^{-1}) and lower cost.[3,4] However, the practical application of LSBs requires

overcoming important challenges. First, the electrical insulating character of sulfur and lithium sulfides involves a poor utilization of the active material.[5] Besides, the severe volumetric variation (~80%) during charge/discharge processes leads to the rapid degradation of the electrode integrity.[1] Moreover, the diffusion of soluble lithium polysulfides (LiPS) intermediates into the electrolyte results in poor cycling stability and low Coulombic efficiency.[6] Additionally, the LiPS conversion reaction is generally characterized by slow redox kinetics, limiting the LSBs charge/discharge rate.[7]

Several strategies have been developed to improve the electrochemical performance of LSBs. In terms of materials, one effective approach is to host sulfur at the cathode in carbon-based materials with high conductivity, such as porous structures of graphene,[8] carbon spheres,[9] carbon nanotubes,[10] and nanofibers.[11] These carbon-based materials can accelerate electron transfer, but are not able to suppress LiPS shuttling due to a weak chemical interaction between nonpolar carbons and polar LiPS. Therefore, LSBs based on carbon suffer from serious capacity fading.[12] On the other hand, polar materials, such as TiO_2 and MnO_2, strongly bind LiPS and efficiently confine LiPS to the cathode, achieving notable improvements in cycling stability.[13,14] However, such semiconducting oxides are characterized by insufficient electrical conductivities, what results in inferior rate capabilities. In terms of structure, hollow nanomaterials, like nanotubes, nanospheres or nanocubes, have been demonstrated advantageous in LSBs because of their large pore volumes and surface-to-volume ratios, which mitigate the detrimental effect of the volume expansion and provide an effective physical confinement for LiPS.[5,15] Besides, the use of electrocatalysts have been demonstrated effective to accelerate the conversion of soluble long-chain LiPS into

solid phases of sulfur and Li_2S_2/Li_2S.[16–18] Overall, high performance LSB cathodes require materials with excellent electrical conductivity, significant polarity to ensure a strong polysulfide affinity, high catalytic activity toward sulfide redox reactions and with hollow nanostructures to relieve volumetric expansion during charge/discharge (as shown in TOC).

Transition metal sulfides/selenides (TMS/TMSe) have attracted much attention for energy storage in recent years. TMS (e.g. CoS_2, VS_2) have been proved as efficient catalysts in several energy conversion fields such as photovoltaics, solar-light to fuel photoconversion and electrochemical hydrogen evolution.[19,20] Their high catalytic activity has been related to the abundance of defects on the surface of TMS due to the moderate electronegativity differences between transition metals and sulfur, the variable oxidation state of sulfur, and the potential formation of sulfur-sulfur and also metal-metal bonds.[21,22] TMS are also highly stable catalysts in reactions involving sulfur.[23] Besides, TMS have shown a strong bonding ability for LiPS owing to their polar character.[17,24] TMSe display similar crystallographic structures, high defect densities and polar character to TMS owing to the relatively similar electronegativity and ionic radius of S and Se . However, the electrical conductivity of TMSe is much higher than the corresponding TMS. Se is characterized by electrical conductivities (1×10^{-3} S m^{-1}) many orders of magnitude higher than S (5×10^{-28} S m^{-1}).[25] Thus, it is reasonable to speculate that TMSe would be promising hosts for LSBs because of their polarity, potential high catalytic activity, and high electrical conductivity. To our knowledge, this is the first work in which bimetallic selenides are reported as S host for LSBs.

$NiCo_2Se_4$ (NCSe) was specifically selected as the host material owing to its metallic nature and synergistic effect between Ni/Co atoms.[26,27] The compound was prepared in the form of

urchin like structures through a two-step hydrothermal process. We thoroughly studied the performance of LSBs based on urchin-like NCSe (u-NCSe) both experimentally and though theoretical calculations. Results presented in this manuscript show the benefits of a highly conductive and polar bimetallic selenide with a tubular structure for rapid electron transfer, enhanced confinement of LiPS, mitigation of volume expansion effects, and a catalytic enhancement of the electrochemical reaction kinetics.

2. Results and Discussion

The synthesis strategy to produce S@u-NCSe is schematically shown in **Figure 1** (details can be obtained in the experimental section). u-NCSe was produced using two hydrothermal reaction steps.[7,28] In the first step, $Ni_{0.33}Co_{0.67}(CO_3)_{0.5}OH$ urchin-like particles having an average diameter of 8-10 μm and containing solid nanoneedles of 200 nm diameter were produced (**Figure 2**a and S1).[28] In a second step, such precursor nanostructures were selenized to u-NCSe (Figure 2b and 2c), which crystallized in the $NiCo_2Se_4$ phase, as indicated by XRD (JCPDS No. 81-4821) and HRTEM characterization (Figure 2e and 2h).[27] u-NCSe displayed hollow tubular structures as observed from SEM and TEM micrographs (Figure 2c and 2d). The hollow structure was originated from the differential diffusivity of the metals and selenium through the growing $NiCo_2Se_4$ shell, *via* the nanoscale Kirkendall effect.[29,30] The surface of the u-NCSe nanotubes is very rough, which translates into high effective surface areas and provides additional sites for electrochemical reactions as compared to the bulk counterpart (b-NCSe, Figure S2). Within the experimental error, energy dispersive spectroscopy (EDS) and electron energy loss spectroscopy (EELS) elemental maps showed the relative atomic content of Ni, Co and Se to match well with stoichiometric $NiCo_2Se_4$, with the three elements homogeneously distributed within u-NCSe (Figure 2f and 2g).

X-ray photoelectron spectroscopy (XPS) spectra of the samples exposed to air are shown in Figure S3. Ni 2p and Co 2p spectra display two pairs of spin-orbit doublets, $2p_{3/2}$ and $2p_{1/2}$, and two shake-up satellite peaks (marked "Sat.").[31] In the Ni 2p spectra (Figure S3 a), the peaks located at 853.6 eV (Ni $2p_{3/2}$) and 871 eV (Ni $2p_{1/2}$) are assigned to Ni^{2+}, and the peaks at 856.3 eV (Ni $2p_{3/2}$) and 874.2 eV (Ni $2p_{1/2}$) to Ni^{3+}.[28] Similarly, in the Co 2p spectra

(Figure S3 b), the peaks located at 778.9 eV (Co $2p_{3/2}$) and 793.9 eV (Co $2p_{1/2}$) are related to Co^{3+} and those at 781.2 eV (Co $2p_{3/2}$) and 797.5 eV (Co $2p_{1/2}$) to Co^{2+}.[28] Se 3d peaks are located at 59.3 (Se $3d_{3/2}$) and 54.8 eV (Se $3d_{5/2}$) in agreement with Se^{2-} in a metal selenide environment (Figure S3 c).[32] The XPS spectra show the presence of occupied states at the Fermi level as it corresponds to a metal or a highly degenerated semiconductor (Figure S3 d). Additionally, the calculated band structure and density of states of NCSe showed no gap of states at the Fermi level, demonstrating its metallic character (Figure 2i).[27]

Sulfur was introduced within u-NCSe by a melt-diffusion process (see experimental section for details). The product or S@u-NCSe morphology resembles the original urchin-like structure of u-NCSe (**Figure 3**a and 3b), but with the hollow structure partially filled with sulfur. Attempts to completely fill the tubes with sulfur were not considered since we believe that remaining internal voids in the porous structure are advantageous to accommodate the volumetric change during the charge/discharge process and trap polysulfides, favoring the cycling stability.[33] XRD analysis demonstrates the presence of crystalline cubic sulfur (JCPDS No. 08-0247) within the S@u-NCSe nanocomposite (Figure 3c) and the retention of the $NiCo_2Se_4$ crystal structure.[7] S@u-NCSe contains ca. 70 wt.% of sulfur as measured by thermogravimetric analysis (TGA, Figure 3d). In addition, with the incorporation of sulfur, the value of Brunauer-Emmett-Teller (BET) specific surface area reduced from 22.4 $m^2 g^{-1}$ (u-NCSe) to 1.7 $m^2 g^{-1}$ (S@u-NCSe), and the overall pore volume decreased from 0.20 $cm^3 g^{-1}$ to 0.017 $cm^3 g^{-1}$, indicating the successful filling of the u-NCSe porous structure by S (Figure S4). Four-point probe method was applied to obtain electrical conductivities of the host materials before and after sulfur fusion (Figure S5). u-NCSe and b-NCSe exhibited

relatively high electrical conductivities, 287.7 and 295.1 S cm^{-1}, respectively, well above that of Super P (9.5 S cm^{-1}).[34] After fusion with sulfur, S@u-NCSe showed electrical conductivities up to of 24.4 S cm^{-1}, well above that of S@b-NCSe (16.9 S cm^{-1}) and nearly six-fold above that of S@Super P (3.9 S cm^{-1}). The higher electrical conductivity of S@u-NCSe compared to S@b-NCSe can be explained by the hollow tubular nanostructure, which allows storing a large amount of sulfur but partially conserving a network of avenues for charge transport.

The material adsorption ability plays a vital role in the confinement of LiPS. We tested this adsorption ability by immersing 20 mg of u-NCSe into a LiPS (~Li_2S_4, 10 mM) solution. For comparison the same test was carried out with b-NCSe and also with Super P, a carbon material typically used as an electrode additive. Upon immersion, clear differences in color were observed in as-prepared solutions (**Figure 4**a). This color change was quantitatively followed by UV-vis spectroscopy, monitoring the absorbance intensity in the 400-500 cm^{-1} region associated to Li_2S_4 (Figure 4b).[35–37] The color of Li_2S_4 solution after the addition of u-NCSe and b-NCSe was much lighter than that of the solution containing Super P, inferring a stronger chemical interaction of LiPS with NCSe.[38] The color of the solution containing u-NCSe was clearer than that of b-NCSe, most probably due to the much higher surface area of the former. The colors of the solutions with or without addition of Super P were nearly the same, indicating the weak Li_2S_4 adsorption ability of Super P.

XPS analysis confirmed the strong interaction of LiPS with NCSe. Figure 4c and 4d exhibit high-resolution Ni $2p_{3/2}$ and Co $2p_{3/2}$ XPS spectra of u-NCSe before and after adsorption test. The last denoted as u-NCSe/Li_2S_4. Compared with the original Ni $2p_{3/2}$and Co $2p_{3/2}$ spectra,

electron binding energies in u-NCSe/Li_2S_4 shifted to higher values, indicating the interaction of S with surface Ni and Co.[39]

We further verified the strong interaction between NCSe and intermediate LiPS species by density functional theory (DFT). Figure S6 exhibits the binding energies and atomic structures between LiPS (Li_2S_2, Li_2S_4, Li_2S_6) and the (110) and (001) surfaces of NCSe. Figure 4e displays the relaxed adsorption structure of Li_2S_4 on the two selected NCSe facets. Li preferentially binds to Se sites and S to Ni and Co ions. Compared with the previous reports on graphitic carbon,[40] the lower sulfur binding energies on the surface of NCSe (Figure 4f) indicates a stronger adsorption of soluble LiPS, which favors an enhanced electrochemical performance. Interestingly, (110) surface shows lower binding energies than (001) surface, demonstrating a higher anchor strength to soluble LiPS of the former.

To better understand the role of Ni and Co within u-NCSe, we produced and characterized the structural and functional properties of the selenides of the constituent elements. XRD patterns of Ni and Co selenides matched well with NiSe and Co_3Se_4 crystal phases (Figure S7 e and f). Figure S7 shows the dandelion-liked NiSe (and its precursor) and nanoneedle-shaped Co_3Se_4 (and its precursor) produced from the same process used to obtain u-NCSe.[28] Notice the geometry of the elemental selenides significantly differed from that of u-NCSe, which can be considered a first main effect of combining both elements into a selenide. u-NCSe was characterized by higher electrical conductivities than NiSe and Co_3Se_4 (Figure S7 g), which is explained by a synergistic effect between the two transition metals, Ni and Co, as reported previously.[27,41,42] Besides, u-NCSe presented much higher LiPS adsorbabilities as displayed in Figure S7 h. This higher adsorbability can be explained by a higher concentration of

defects in the bimetallic selenide, which could act as adsorption/catalytic sites.[43,44] Overall, the combination of Ni and Co within a single selenide structure influence the morphology of the obtained materials and increased electrical conductivity and LiPS adsorbability.

Cyclic voltammetry (CV) tests in symmetric cells using an electrolyte containing 0.5 mol L^{-1} Li_2S_6 and 1 mol L^{-1} LiTFSI dissolved in DOL/DME (v/v = 1/1) were carried out to study the electrocatalytic activity of u-NCSe, b-NCSe and Super P (see details in the experimental section). As illustrated in **Figure 5**a, u-NCSe and b-NCSe electrodes displayed two pairs of reversible redox peaks, named I, II, III, and IV, and associated to the following forward and reverse chemical reactions, respectively:[16]

Peaks I and III: $S_6^{2-} + 10e^- + 12Li^+ \leftrightarrow 6Li_2S$

Peaks II and IV: $3S_8 + 8e^- \leftrightarrow 4S_6^{2-}$

On the contrary, the linear-shaped CV of Super P did not show evident redox behavior. u-NCSe-based cells provided the highest peak current densities, indicating higher redox activity and accelerated reaction kinetics during liquid-to-solid ($Li_2S \leftrightarrow S_6^{2-} \leftrightarrow S_8$) conversion.[38,39] This higher activity should have associated a reduction of soluble LiPS in the electrolyte, having a positive influence in the cycling stability of u-NCSe-based cells, as shown below. Besides, the CV curve of u-NCSe without Li_2S_6 addition exhibited a nearly rectangular shape (Figure S8) that indicated a pure capacitive contribution, thus pointing at Li_2S_6 as the unique electrochemically active specie. Electrochemical impedance spectroscopy (EIS) analysis of symmetric cells showed NCSe samples to be characterized by much lower charge transfer resistance (Rct) than Super P, i.e. a much faster charge transfer at the NCSe-polysulfide interface than at Super P-polysulfide interface (Figure 5b).[16,46]

CV curves of Li-S coin cells based on S@Super P, S@b-NCSe and S@u-NCSe containing similar amounts of S (Figure S9 and S10) were shown in Figure 5c. Two cathodic peaks (peak I and peak II) were identified during reduction of S_8 into long-chain LiPS (Li_2S_x, $4< x < 8$) and their subsequent conversion to insoluble products (Li_2S_2 and Li_2S), respectively. The anodic peak (peak III) accounts for the multistep oxidation conversion of short-chain Li_2S_2/Li_2S to LiPS and eventually to sulfur.[46] Reduction peaks measured from cells based on S@u-NCSe systematically exhibited the highest potentials (peak I at 2.32 and peak II at 2.07 V) and current densities among the different materials tested (S@b-NCSe at 2.26 and 2.02 V, S@Super P at 2.2 and 1.92V), as shown in Figure 5d. However, the peak voltage and onset potential of oxidation peaks displayed inverse results, indicating that u-NCSe can effectively increase the polysulfides redox reaction kinetics.[17,47] Besides, the enhanced catalytic activity of u-NCSe was also confirmed by changes in onset potentials, taken at a current density of 10 μA cm^{-2} beyond the baseline current (Figure S11). As illustrated in Figure 5d, among the three kinds of electrode tested, S@u-NCSe exhibited the highest onset potentials of reduction peaks and the lowest onset potentials of oxidation peaks, evidencing the capacity of u-NCSe to electrocatalytically accelerate the reaction kinetics.[17,48] CV curves of S@u-NCSe (Figure S12 a) almost overlapped in the first cycle, showing no obvious peak shifts or current changes, which indicated good stability and high reversibility.[49]

The lithium ion diffusion coefficient was evaluated qualitatively from CV tests under different scanning rates, in the range from 0.1 mV s^{-1} to 0.4 mV s^{-1} (Figure 5e and 5f). A linear relationship was obtained between the reduction and oxidation peak currents and the square root of scanning rates, demonstrating the reaction to be diffusion-limited. Thus the lithium ion

diffusivity can be calculated using the classical Randles-Sevcik equation:[38,47]

$$I_p = (2.69 \cdot 10^5) n^{1.5} A D_{Li^+}{}^{0.5} C_{Li^+} v^{0.5}$$

where I_p is the peak current, n is the number of charge transfer, A is the geometric electrode area, D_{Li}^+ is the lithium ion diffusion coefficient, C_{Li}^+ is the concentration of lithium ions in the cathode, and v is the scan rate. S@u-NCSe electrodes showed the sharpest slopes (Figure S13), thus the highest lithium ion diffusivity. We hypothesize this higher lithium ion diffusivity to be related to the relief of the shuttle effect and the improved catalytic activity of the u-NCSe host towards LiPS conversion demonstrated above, avoiding the high viscosity electrolyte caused by LiPS dissolution and the deposition of a thick insulating layer on the electrode.[38]

During charge/discharge processes, the overpotential of LSBs was mainly caused by the sluggish kinetics of the oxidation/reduction of insulated solid Li_2S.[38,39,50] To further demonstrate the catalytic effect of u-NCSe, Li_2S nucleation and dissolution experiments were conducted with a Li_2S_8/DOL-DME solution (details can be found in experimental section).[51] Figure 5g shows potentiostatic discharge profiles that demonstrate that CP/u-NCSe electrodes displayed faster responsivity toward Li_2S nucleation than CP/Super P. Based on the Faraday's law, CP/u-NCSe electrodes also exhibited larger capacities of Li_2S precipitation (151.1 mAh g $^{-1}$) and shorter nucleation and growth times than CP/Super P electrodes (74.6 mAh g^{-1}). These results demonstrate that u-NCSe hosts can significantly reduce overpotential for the initial Li_2S nucleation and promote kinetics for subsequent Li_2S precipitation.[52–54] A similar strategy was used to study the kinetics of Li_2S dissolution (Figure 5h). Potentiostatic charge curves of CP/u-NCSe exhibited higher current densities than CP/Super P, indicating a lower

oxidation overpotential for Li_2S dissolution. Moreover, the calculated dissolution capacity of CP/u-NCSe (743 mAh g^{-1}) was much higher than for CP/Super P electrodes (389 mAh g^{-1}). Overall, these results verified the superior electrocatalytic effect of u-NCSe hosts in reducing polarization and promoting redox kinetics of LiPS conversion reaction.[39]

Electrochemical performance was further analyzed through galvanostatic charge-discharge tests (**Figure 6**). Charge-discharge curves of S@Super P, S@b-NCSe and S@u-NCSe at 0.1 C showed one charge plateau and two discharge plateaus, consistently with CV. S@u-NCSe showed lower polarization potential (ΔE= 152 mV) than S@b-NCSe (ΔE= 205 mV) and S@Super P electrodes (ΔE= 222 mV).[17,46] The voltage gap ΔE between the oxidation and the second reduction plateaus introduced a hysteresis in the redox reaction.

Discharge curves showed two plateaus, corresponding to the reduction of sulfur to soluble LiPS ($S_8 \rightarrow S_6^{2-} \rightarrow S_4^{2-}$) and the subsequent conversion to insoluble products ($S_4^{2-} \rightarrow Li_2S_2 \rightarrow Li_2S$). The associated capacity of the two discharge plateaus was defined as Q1 and Q2, respectively (Figure 6a). The ratio between Q2 and Q1 (Q2/Q1) can be interpreted in terms of the catalytic ability for LiPS conversion reaction: sluggish kinetics during the solid→liquid→solid process and shuttle effect caused by diffusion of soluble LiPS give rise to capacity fading during Q2 stage. Thus, the higher Q2/Q1, the better catalytic ability.[25,55] As shown in Figure 6b, the Q2/Q1 of S@u-NCSe was 2.8, much higher than that of S@b-NCSe (2.32) and S@Super P (1.88). This high ratio also proved the superior catalytic activity towards polysulfides redox reaction of u-NCSe.

Associated with the ability of u-NCSe to accelerate the charge transfer and promote

conversion of polysulfides, S@u-NCSe showed the largest capacity among the different electrodes tested. All discharge curves at different current rates exhibited two evident discharge plateaus (Figure 6c). The electrochemical capacity of the cell with S@u-NCSe at various current densities from 0.1 C to 5 C is shown in Figure 6d. The initial discharge capacity was 1403 mAh g^{-1}, and stabilized to an average capacity of 1330 mAh g^{-1} at 0.1 C. Even at high current rates of 5 C, the capacity still remained stable at 626 mAh g^{-1}, which is significantly higher than the one obtained for S@Super P electrodes (5 mAh g^{-1}, Figure S14) under the same conditions. Moreover, when the current rate was turned back to 0.2 C, the average capacity of the cell with S@u-NCSe returned to the same approximate value of 1060 mAh g^{-1}, implying a remarkable electrochemical stability.[7,56]

Energy efficiency, the ratio of energy output/input ($E = \int UI\ dt$) upon voltage polarization cycles, is a pivotal parameter in large-scale electrochemical energy storage systems.[17] S@u-NCSe electrodes were characterized with much higher and stable energy efficiencies than S@Super P, especially at high current rates (Figure 6e). As an example, S@u-NCSe retained 85.6% efficiency at 5 C, much higher than the 71.3% for S@Super P. The significant improvement in energy efficiency arised from the lower polarization potential, associated with the exceptional catalytic properties of u-NCSe, as discussed above.

EIS analyses were carried out to gain understanding of the enhanced electrochemical performance of S@u-NCSe electrodes. Figure 6f shows the Nyquist plot obtained from a fresh S@u-NCSe coin cell and the same cell after 100 cycles at 1 C. In the high frequency region, the fresh electrode showed a semicircle corresponding to the charge-transfer resistance, and a linear dependence in the low frequency region that reflected the diffusion of lithium

ions into the electrode. After 100 cycles, the impedance plot changed to two poorly-resolved semicircles at high and middle frequencies and a lineal dependence at low frequencies. [57,58] Apparently, the charge-transfer resistance decreased after cycling, which should be associated with the activation process. Moreover, comparing with the other two types of electrode tested, S@b-NCSe and S@Super P (Figure S15), S@u-NCSe electrodes showed the lowest charge-transfer resistance (Rct).

The long-term cycling stability of the NCSe-based batteries was evaluated at a high current density of 3C (Figure 6g). After 2000 cycles, S@u-NCSe electrodes delivered a capacity of 480 mAh g^{-1}, involving a 0.016% average capacity decay per cycle. Meanwhile, a high and steady Coulombic efficiency above 99.7% was obtained. It is worth mentioning that a negligible capacity was obtained from pure u-NCSe under the same measuring conditions, as shown in Figure S16. In contrast, S@Super P electrodes delivered a considerably low capacity after 400 cycles (294 mAh g^{-1}), suffering from a rapid capacity fading (0.11% average capacity decay per cycle), as well as a low Coulombic efficiency (average about 97.1%) at 1 C (Figure S 14c).

For practical applications, high energy density Li-S batteries require increasing the sulfur loading. Therefore, we studied the performance of S@u-NCSe electrodes at a higher sulfur loading, 3.2 mg cm^{-2}. Figure S17a displays galvanostatic charge-discharge curves of a S@u-NCSe electrode at different current rates. One charge plateau and two discharge plateaus were clearly observed at all current rates, up to 3 C, demonstrating the low polarization between charge and discharge processes. At this high sulfur loading, we measured average reversible capacities of S@u-NCSe electrodes from 1169 mAh g^{-1} at 0.1 C to 522.8 mAh g^{-1}

at 3 C, which corresponded to areal capacities of 3.65 and 1.63 mAh cm^{-2}, respectively. This high rate performances even at high sulfur loadings was consistent with the high electrical conductivity and superior catalytic properties of this material. Long term cycling tests at 1 C showed S@u-NCSe electrodes loaded with 3.2 mg cm^{-2} of sulfur to maintain 557 mAh g^{-1} after 600 cycles, *i.e.* a 74.3% capacity retention, involving a 0.043% average capacity decay per cycle. Additionally, a high and steady Coulombic efficiency above 98.8% was consistently obtained (Figure 6h), indicating an excellent cycling stability.

Electrochemical results of S@u-NCSe cathodes for LSBs are compared to other state-of-art TM-based materials in Table S1. To illustrate the favorable electrochemical performance of S@u-NCSe cathodes and the promising practical application of related LSBs, one S@u-NCSe coin cell was used to light up a “LSB”-shaped LED panel containing 47 LEDs (voltage: 2-2.2V), as shown in Figure 6i.

Finally, to further demonstrate that u-NCSe effectively confines LiPS and minimizes the shuttle effect in LSBs, coin cells were disassembled after 200 cycles at 1C to inspect their membrane, cathodic integrity and anodic corrosion. Separators from S@u-NCSe coin cells exhibited much lighter color compared to those from S@Super P (Figure 6k). This observation probed that u-NCSe better confined LiPS, avoiding its diffusion during charge/discharge processes.[7,59] Consistently with the lighter color of the separator, Li metal foils from S@u-NCSe coin cells showed less corrosion and fewer Li_2S species deposited at their surface than S@Super P coin cells, as shown by SEM and EDS analyses in Figure 6k and 6l.[48] Thus, the use of u-NCSe as host cathode material greatly relieved the LiPS shuttle effect and minimizes the irreversible losses of active sulfur in LSBs, leading to a superior

stability during long term cycling, Figure 6g. Besides, the crystal structure and morphology of S@u-NCSe after cycling was analyzed. HAADF-STEM and SEM micrographs showed the original tubular nanostructure to be conserved after the cycling (Figure 6j and 6l). Additionally, HRTEM and XRD analysis probed the NCSe crystal structure to be conserved (Figure 6j and S18), indicating an excellent stability towards lithiation/delithiation cycles.

Biological security is an important parameter for application of energy storage materials. Thus, we analyzed the biocompatibility of S@u-NCSe by measuring through MTT assays the cytotoxicity of this material against the human hepatocellular carcinoma cell line HepG2 (please refer to Supporting Information for details).[60] Figure S19 showed the viability of the cultured cells in the presence of S@u-NCSe at concentrations ranging from 0.001 to 1000 μg/mL. Even though a gradual decreasing trend was observed with increasing concentrations, cell viabilities above 85% even at S@u-NCSe concentration of 1000 μg/mL were obtained, indicating that S@u-NCSe composites have a negligible cytotoxicity.

3. Conclusions

In summary, we developed urchin-like $NiCo_2Se_4$ nanostructures serving as polar host with catalytic effect for cathode of LSBs. Comprehensive kinetic investigations revealed that u-NCSe promoted redox kinetics of LiPS conversion reaction, and effectively decreased polarization during charging and discharging processes. A strong LiPS adsorbability was confirmed simultaneously by experimental results and DFT calculations. u-NCSe were characterized by a beneficial hollow structure to relieve volumetric expansion and a superior electrical conductivity to improve electron transfer. Owing to these excellent qualities,

S@u-NCSe delivered impressive rate performance with 1330 and 626 mA h g^{-1} at 0.1 C and 5 C, respectively. More significantly, a reversible capacity of 480 mA h g^{-1} was retained after 2000 cycles at 3 C and, even at high sulfur loading (3.2 mg cm^{-2}), 557 mA h g^{-1} capacity was delivered after 600 cycles at 1 C. Additional cytotoxicity measurements demonstrated the u-NCSe biocompatibility. This work provides a strategy for the rational design and development of LSBs with long-life and high-rate performance in addition to insights into transition metal selenides as sulfur host material.

4. Experimental

Synthesis of u-NCSe. u-NCSe was synthesized by a two-step synthesis process, from selenization of $Ni_{0.33}Co_{0.67}(CO_3)_{0.5}OH$ precursor obtained by a simple hydrothermal process. First, 5 mM $NiCl_2{\cdot}6H_2O$ (98%, Alfa Aesar) and $CoCl_2{\cdot}6H_2O$ (98%, Alfa Aesar) with molar ratio of 1:2 were dissolved into 30 mL of deionized (DI) water, and then 300 mg of urea (99%, Acros Organics) added, using an ultrasounds bath for 3 mins to form a homogeneous solution. This solution was then poured into a Teflon lined stainless steel autoclave of 50 mL volume and heated at 130 °C for 8 h. After naturally cooling to ambient temperature, the $Ni_{0.33}Co_{0.67}(CO_3)_{0.5}OH$ precipitate was centrifuged, washed, dried and recovered. Subsequently, 50 mg of as-obtained $Ni_{0.33}Co_{0.67}(CO_3)_{0.5}OH$ were dispersed in 25 mL of deionized water using an ultrasonic bath and then 150 mg of Na_2SeO_3 (99%, Alfa Aesar) and 4 mL of $N_2H_4{\cdot}H_2O$ (98%, Sigma Aldrich) were incorporated under vigorous stirring. The mixture was finally poured into a Teflon-lined stainless steel autoclave of 50 mL volume and heated at 180 °C for 8 h. After cooling naturally to ambient temperature, the precipitate was centrifuged, washed, dried and recovered. NiSe and Co_3Se_4 nanostructures were synthesized

following the same synthesis protocol.

Synthesis of b-NCSe. b-NCSe was obtained in just one synthesis step. 37 mg of $NiCl_2 \cdot 6H_2O$, 75 mg of $CoCl_2 \cdot 6H_2O$ and 150 mg of Na_2SeO_3 were dissolved into 25 mL of deionized water and then 4 mL of $N_2H_4 \cdot H_2O$ were dropped into the solution under vigorous stirring conditions. The resulting solution was finally poured into a Teflon-lined stainless steel autoclave of 50 mL volume and heated at 180 °C for 8 h.

Synthesis of S@u-NCSe and S@b-NCSe. u-NCSe and sulfur powder (99.98%, Sigma Aldrich) (1:3, weigh ratio) were mixed and heated at 155 °C for 12 h in a glass bottle under Ar atmosphere. In order to remove the redundant sulfur not incorporated into u-NCSe, the powder was immersed in a 10 mL CS_2 and ethanol solution (1:4, volume ratio) for 10 min twice. S@b-NCSe was obtained using the same process.

Synthesis of S@Super P. Super P (99%, Alfa Aesar) and sulfur powder (3:7, weigh ratio) were well mixed and heated at 155 °C for 12 h.

Materials Characterization: X-ray diffraction (XRD) patterns were recorded at room temperature using a Bruker AXS D8 Advance X-ray diffractometer with Cu K radiation (λ = 1.5106 Å) operating at 40 kV and 40 mA. The morphology and microstructure were examined by TEM (ZEISS LIBRA 120) and FESEM (ZEISS Auriga) equipped with an energy dispersive X-ray spectroscopy (EDS) detector operated at 20 kV. High-resolution TEM (HRTEM) and scanning TEM (STEM) studies were carried out using a field emission gun FEI Tecnai F20 microscope at 200 kV with a point-to-point resolution of 0.19 nm. High angle annular dark-field (HAADF) STEM was combined with electron energy loss spectroscopy (EELS) in the Tecnai microscope by using a GATAN QUANTUM filter. X-ray photoelectron

spectroscopy (XPS) measurements were carried out in normal emission using an Al anode XR50 source operating at 150 mW and a Phoibos 150 MCD-9 detector. TGA (PerkinElmer Diamond TG/DTA instrument.) experiments were performed to estimate the content of S in prepared composites. The specific surface area and analysis of the pore size distribution were performed by Brunauer-Emmett-Teller method (Tristar II 3020 Micromeritics system). UV-vis absorption spectra were recorded on a PerkinElmer LAMBDA 950 UV-vis spectrophotometer. Electrical conductivities were measured using a four-point probe station (Keithley 2400, Tektronix).

Li-S cell assembly and measurements. S@host composites (S@u-NCSe; S@b-NCSe; S@Super P), Super P and PVDF binder (weight ratio = 8:1:1) were dispersed in N-methyl pyrrolidone (NMP, 99.5%, Acros Organics) to form a slurry which was coated on aluminum foils and dried at 60 °C overnight. The coated aluminum foil was then punched into small disks with a diameter of 12.0 mm. Sulfur loading was about 1.0-1.1 mg cm^{-2}. High-loading tests were applied using 3.2 mg cm^{-2} of sulfur. Electrochemical measurements were conducted in standard 2032 coin-type cells. In LSBs assemblies, lithium foils were used as counter electrode and Celgard 2400 membranes as separators. The electrolyte used was 1.0 M lithium bis(trifluoromethanesulfonyl)imide (LiTFSI) (99%, Acros Organics) dissolved in a mixture of 1,3-dioxolane (DOL, 99.5%, Alfa Aesar) and 1,2-dimethoxy ethane (DME, 99%, Honeywell) (v/v = 1/1) and containing 0.2 M of $LiNO_3$ (99.98%, Alfa Aesar). For each coin cell, 20 μL of electrolyte was used, high-loaded coin cells added 45 μL. The cells were galvanostatically cycled within a voltage range of 1.7-2.8 V using a Neware BTS4008 battery tester at different C rates. Cyclic voltammetry (CV) measurements were performed on a

battery tester BCS-810 from Bio Logic at a scan rate of 0.1-0.4 mV s^{-1} and electrochemical impedance spectroscopy (EIS) tests were performed using a sinusoidal voltage with amplitude of 10 mV in the frequency range 100 kHz to 10 mHz.

Preparation of Li_2S_x (like Li_2S_4, Li_2S_6, Li_2S_8, x=4, 6 or 8) solutions for adsorption test and kinetic study. Sulfur and Li_2S (99.9%, Alfa Aesar) in the molar ratio x-1:1 were added to appropriate amounts of DME and DOL (volume ratio of 1:1) under vigorous magnetic stirring overnight until a dark brown solution was formed. 20 mg of Super P, b-NCSe or u-NCSe were poured into 3.0 mL 10 mM Li_2S_4 solution, respectively, and mixtures stirred for homogenization overnight.

Symmetric cell assembly and measurements. Electrodes for symmetric cells were fabricated in the same way as electrodes for LSBs. Two pieces of the same electrode (average loading about 0.5 mg cm^{-2}) were used as identical working and counter electrodes with 40 µL of electrolyte containing 0.5 mol L^{-1} Li_2S_6 and 1 mol L^{-1} LiTFSI dissolved in DOL/DME (v/v = 1/1). For comparison, symmetric cells with electrolyte 1 mol L^{-1} LiTFSI dissolved in DOL/DME (v/v = 1/1) were also assembled and tested. In all cases, CV measurements were performed at scan rate of 40 mV s^{-1}.

Measurement of nucleation and dissolution of Li_2S.

The nucleation and dissolution of Li_2S were tested in 2032 coin cells, where 1 mg of u-NCSe or Super P loaded on the carbon papers was applied as work electrode, Li foil worked as the counter electrode, 20 µL of 0.25 M Li_2S_8 dissolved in DOL/DME (v/v=1:1) solution with 1.0 M LiTFSI was used as catholyte, and 20 µL of 1.0 M LiTFSI in DOL/DME (v/v=1:1) solution solution as anolyte. The cells were held at 2.19 V for 2 h to reduce higher order LiPS to Li_2S_4.

And then held them at potential of 2.05 V until current decreased to 10^{-2} mA for Li_2S nucleation and growth.[51] In order to analyze the Li_2S dissolution, fresh cells were first discharged at a current of 0.10 mA to 1.80 V, and subsequently discharged at 0.01 mA to 1.80 V for full transformation of S species into solid Li_2S. After this discharge, cells were potentiostatically charged at 2.40 V for the dissolution of Li_2S into LiPS until charge current was below 10^{-5} A.[39]

Supporting Information
Supporting Information is available from the Wiley Online Library or from the author.

Acknowledgements
This work corresponds to an extension of activities initially performed around the objectives defined by the Helis project which received funding from the European Union's Horizon 2020 program under the Grant Agreement No 666221. Authors acknowledge funding from Generalitat de Catalunya 2017 SGR 1246 and 2017 SGR 327, the Spanish MINECO projects ENE2016-77798-C4-3-R and ENE2017-85087-C3, and the Zhou Shan Science and Technology Project (2018C21010). C. Zhang and T. Zhang thank the China Scholarship Council (CSC) for scholarship support. IREC acknowledges funding from European Regional Development Funds (ERDF-FEDER Programa Competitivitat de Catalunya 2007-2013). ICN2 is supported by the Severo Ochoa program from Spanish MINECO (Grant No. SEV-2017-0706) and is funded by the CERCA Programme/Generalitat de Catalunya. Part of the present work has been performed in the framework of Universitat Autònoma de Barcelona Materials Science PhD program.

Conflicts of interest
There are no conflicts to declare.

Received: ((will be filled in by the editorial staff))
Revised: ((will be filled in by the editorial staff))
Published online: ((will be filled in by the editorial staff))

References

[1] Z. W. Seh, Y. Sun, Q. Zhang, Y. Cui, *Chem. Soc. Rev.* **2016**, *45*, 5605.

[2] X. Ji, K. T. Lee, L. F. Nazar, *Nat. Mater.* **2009**, *8*, 500.

[3] H.-J. Peng, J.-Q. Huang, X.-B. Cheng, Q. Zhang, *Adv. Energy Mater.* **2017**, 1700260.

[4] A. Manthiram, Y. Fu, S.-H. Chung, C. Zu, Y.-S. Su, *Chem. Rev.* **2014**, *114*, 11751.

[5] Z. Li, H. B. Wu, X. W. (David) Lou, *Energy Environ. Sci.* **2016**, *9*, 3061.

[6] J. Zhang, H. Huang, J. Bae, S.-H. Chung, W. Zhang, A. Manthiram, G. Yu, *Small Methods* **2018**, *2*, 1700279.

[7] C. Dai, J.-M. Lim, M. Wang, L. Hu, Y. Chen, Z. Chen, H. Chen, S.-J. Bao, B. Shen, Y. Li, G. Henkelman, M. Xu, *Adv. Funct. Mater.* **2018**, *28*, 1704443.

[8] C. Zu, A. Manthiram, *Adv. Energy Mater.* **2013**, *3*, 1008.

[9] B. Zhang, X. Qin, G. R. Li, X. P. Gao, *Energy Environ. Sci.* **2010**, *3*, 1531.

[10] J.-Q. Huang, Q. Zhang, S.-M. Zhang, X.-F. Liu, W. Zhu, W.-Z. Qian, F. Wei, *Carbon* **2013**, *58*, 99.

[11] S. Evers, L. F. Nazar, *Acc. Chem. Res.* **2013**, *46*, 1135.

[12] H.-J. Peng, G. Zhang, X. Chen, Z.-W. Zhang, W.-T. Xu, J.-Q. Huang, Q. Zhang, *Angew Chem Int Ed* **2016**, 15.

[13] Z. Wei Seh, W. Li, J. J. Cha, G. Zheng, Y. Yang, M. T. McDowell, P.-C. Hsu, Y. Cui, *Nat. Commun.* **2013**, *4*.

[14] K. Cao, H. Liu, Y. Li, Y. Wang, L. Jiao, *Energy Storage Mater.* **2017**, *9*, 78.

[15] B.-Q. Li, S.-Y. Zhang, L. Kong, H.-J. Peng, Q. Zhang, *Adv. Mater.* **2018**, *30*, 1707483.

[16] H. Lin, L. Yang, X. Jiang, G. Li, T. Zhang, Q. Yao, G. W. Zheng, J. Y. Lee, *Energy Environ. Sci.* **2017**, *10*, 1476.

[17] Z. Yuan, H.-J. Peng, T.-Z. Hou, J.-Q. Huang, C.-M. Chen, D.-W. Wang, X.-B. Cheng, F. Wei, Q. Zhang, *Nano Lett.* **2016**, *16*, 519.

[18] D. Liu, C. Zhang, G. Zhou, W. Lv, G. Ling, L. Zhi, Q.-H. Yang, *Adv. Sci.* **2018**, *5*, 1700270.

[19] R. Lv, J. A. Robinson, R. E. Schaak, D. Sun, Y. Sun, T. E. Mallouk, M. Terrones, *Acc. Chem. Res.* **2015**, *48*, 56.

[20] Q. H. Wang, K. Kalantar-Zadeh, A. Kis, J. N. Coleman, M. S. Strano, *Nat. Nanotechnol.* **2012**, *7*, 699.

[21] R. R. Chianelli, G. Berhault, B. Torres, *Catal. Today* **2009**, *147*, 275.

[22] C. Coughlan, M. Ibáñez, O. Dobrozhan, A. Singh, A. Cabot, K. M. Ryan, *Chem. Rev.* **2017**, *117*, 5865.

[23] R. R. Chianelli, M. Daage, M. J. Ledoux, In *Advances in Catalysis*; Eley, D. D.; Pines, H.; Haag, W. O., Eds.; Academic Press, 1994; Vol. 40, pp. 177–232.

[24] Z. Cheng, Z. Xiao, H. Pan, S. Wang, R. Wang, *Adv. Energy Mater.* **2018**, *8*, 1702337.

[25] C.-Y. Fan, Y.-P. Zheng, X.-H. Zhang, Y.-H. Shi, S.-Y. Liu, H.-C. Wang, X.-L. Wu, H.-Z. Sun, J.-P. Zhang, *Adv. Energy Mater.* **2018**, *8*, 1703638.

[26] Z. Fang, L. Peng, Y. Qian, X. Zhang, Y. Xie, J. J. Cha, G. Yu, *J. Am. Chem. Soc.* **2018**, *140*, 5241.

[27] Z. Fang, L. Peng, H. Lv, Y. Zhu, C. Yan, S. Wang, P. Kalyani, X. Wu, G. Yu, *ACS Nano* **2017**, *11*, 9550.

[28] X. Qian, H. Li, L. Shao, X. Jiang, L. Hou, *ACS Appl. Mater. Interfaces* **2016**, *8*, 29486.

[29] M. Ibáñez, J. Fan, W. Li, D. Cadavid, R. Nafria, A. Carrete, A. Cabot, *Chem. Mater.* **2011**, *23*, 3095.

[30] A. Cabot, M. Ibáñez, P. Guardia, A. P. Alivisatos, *J. Am. Chem. Soc.* **2009**, *131*, 11326.

[31] Y. Li, L. Xu, M. Jia, L. Cui, J. Gao, X.-J. Jin, *J. Electrochem. Soc.* **2018**, *165*, E303.

[32] Q. Wang, Y. Ma, Y. Wu, D. Zhang, M. Miao, *ChemSusChem* **2017**, *10*, 1427.

[33] Z. Li, J. Zhang, B. Y. Guan, X. Wen, *Angew Chem* **2017**, 16.

[34] L. Long, X. Jiang, J. Liu, D. Han, M. Xiao, S. Wang, Y. Meng, *RSC Adv.* **2018**, *8*, 4503.

[35] T. Lei, W. Chen, J. Huang, C. Yan, H. Sun, C. Wang, W. Zhang, Y. Li, J. Xiong, *Adv. Energy Mater.* **2017**, *7*, 1601843.

[36] J. Song, Z. Yu, M. L. Gordin, D. Wang, *Nano Lett.* **2016**, *16*, 864.

[37] X. Li, K. Ding, B. Gao, Q. Li, Y. Li, J. Fu, X. Zhang, P. K. Chu, K. Huo, *Nano Energy* **2017**, *40*, 655.

[38] G. Zhou, H. Tian, Y. Jin, X. Tao, B. Liu, R. Zhang, Z. W. Seh, D. Zhuo, Y. Liu, J. Sun, J. Zhao, C. Zu, D. S. Wu, Q. Zhang, Y. Cui, *Proc. Natl. Acad. Sci.* **2017**, *114*, 840.

[39] H. Yuan, H.-J. Peng, B.-Q. Li, J. Xie, L. Kong, M. Zhao, X. Chen, J.-Q. Huang, Q. Zhang, *Adv. Energy Mater.* **2018**, 1802768.

[40] Y. Qiu, W. Li, W. Zhao, G. Li, Y. Hou, M. Liu, L. Zhou, F. Ye, H. Li, Z. Wei, S. Yang, W. Duan, Y. Ye, J. Guo, Y. Zhang, *Nano Lett.* **2014**, *14*, 4821.

[41] C. Wu, Y. Wei, Q. Lian, C. Cui, W. Wei, L. Chen, C. Li, *Mater. Chem. Front.* **2017**, *1*, 2656.

[42] C. Xia, H. Liang, J. Zhu, U. Schwingenschlögl, H. N. Alshareef, *Adv. Energy Mater.* **2017**, *7*.

[43] D. Luo, G. Li, Y.-P. Deng, Z. Zhang, J. Li, R. Liang, M. Li, Y. Jiang, W. Zhang, Y. Liu, W. Lei, A. Yu, Z. Chen, *Adv. Energy Mater.* **2019**, 1900228.

[44] C. Xia, Q. Jiang, C. Zhao, M. N. Hedhili, H. N. Alshareef, *Adv. Mater.* **2016**, *28*, 77.

[45] J. Zhou, X. Liu, L. Zhu, J. Zhou, Y. Guan, L. Chen, S. Niu, J. Cai, D. Sun, Y. Zhu, J. Du, G. Wang, Y. Qian, *Joule* **2018**.

[46] L. Zhang, X. Chen, F. Wan, Z. Niu, Y. Wang, Q. Zhang, J. Chen, *ACS Nano* **2018**, *12*, 9578.

[47] X. Zhu, W. Zhao, Y. Song, Q. Li, F. Ding, J. Sun, L. Zhang, Z. Liu, *Adv. Energy Mater.* **2018**, *8*, 1800201.

[48] L. Ma, W. Zhang, L. Wang, Y. Hu, G. Zhu, Y. Wang, R. Chen, T. Chen, Z. Tie, J. Liu, Z. Jin, *ACS Nano* **2018**, *12*, 4868.

[49] Z. Li, Q. He, X. Xu, Y. Zhao, X. Liu, C. Zhou, D. Ai, L. Xia, L. Mai, *Adv. Mater.* **2018**, *30*, 1804089.

[50] A. Berger, A. T. S. Freiberg, A. Siebel, R. Thomas, M. U. M. Patel, M. Tromp, H. A. Gasteiger, Y. Gorlin, *J. Electrochem. Soc.* **2018**, *165*, A1288.

[51] F. Y. Fan, Y.-M. Chiang, *J. Electrochem. Soc.* **2017**, *164*, A917.

[52] Y. Wang, R. Zhang, Y. Pang, X. Chen, J. Lang, J. Xu, C. Xiao, H. Li, K. Xi, S. Ding, *Energy Storage Mater.* **2019**, *16*, 228.

[53] F. Y. Fan, W. C. Carter, Y.-M. Chiang, *Adv. Mater.* **2015**, *27*, 5203.

[54] S. Huang, Y. V. Lim, X. Zhang, Y. Wang, Y. Zheng, D. Kong, M. Ding, S. A. Yang, H. Y. Yang, *Nano Energy* **2018**, *51*, 340.

[55] D. Su, M. Cortie, H. Fan, G. Wang, *Adv. Mater.* **2017**, *29*, 1700587.

[56] J. He, Y. Chen, A. Manthiram, *iScience* **2018**, *4*, 36.

[57] Z. Guo, H. Nie, Z. Yang, W. Hua, C. Ruan, D. Chan, M. Ge, X. Chen, S. Huang, *Adv. Sci.* **2018**, *5*, 1800026.

[58] W. Bao, D. Su, W. Zhang, X. Guo, G. Wang, *Adv. Funct. Mater.* **2016**, *26*, 8746.

[59] L. Hu, C. Dai, H. Liu, Y. Li, B. Shen, Y. Chen, S.-J. Bao, M. Xu, *Adv. Energy Mater.* **2018**, *8*, 1800709.

[60] A. Dirany, I. Sirés, N. Oturan, A. Özcan, M. A. Oturan, *Environ. Sci. Technol.* **2012**, *46*, 4074.

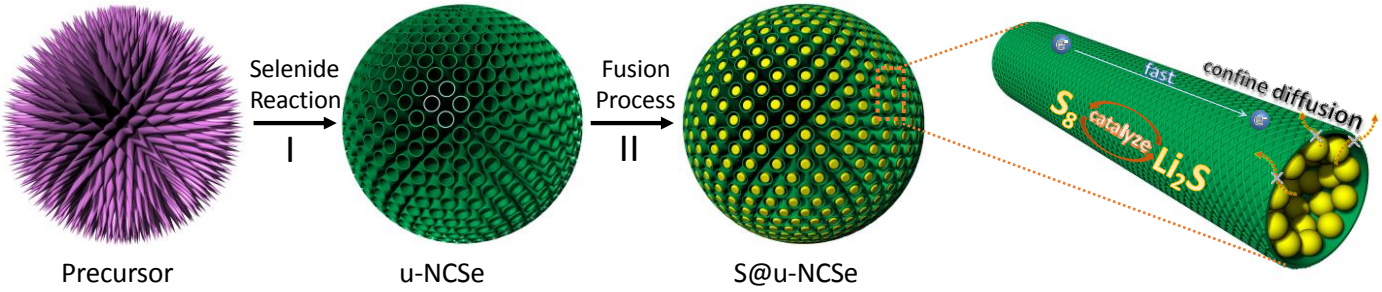

Figure 1. Schematic illustration of the fabrication process of S@u-NCSe composites as cathode for LSBs.

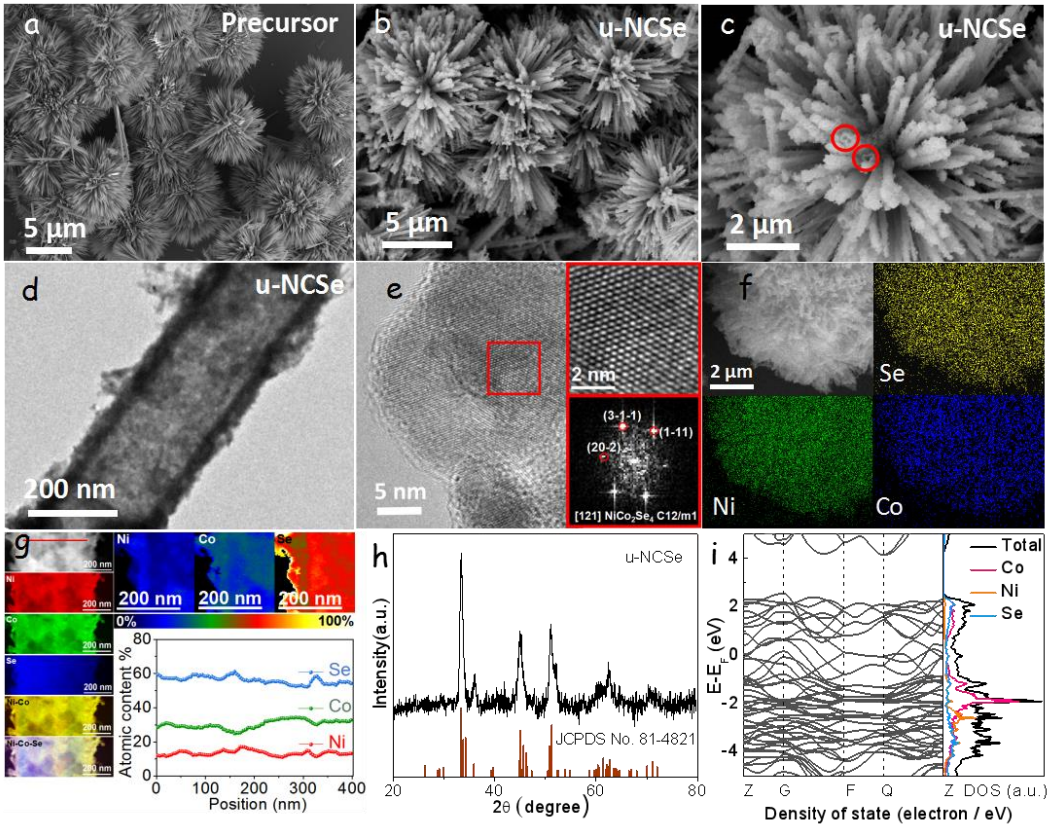

Figure 2. (a) FESEM image of urchin shaped precursor. (b, c) FESEM images and (d) TEM image of u-NCSe. (e) HRTEM image of u-NCSe and inset are images corresponding to FFT spectrum, which indicate that the material crystallizes in the monoclinic $NiCo_2Se_4$ phase, as visualized along the [121] direction. (f) EDX elemental mapping of Ni, Co, and Se elements collected from the selected area. (g) HAADF image and EELS chemical composition maps obtained from the STEM micrograph. Individual Ni L2,3-edges at 855 eV (red), Co L2,3-edges at 779 eV (green) and Se L2,3-edges at 1436 eV (blue) as well as composites of Ni-Co and Ni-Co-Se (Left) are shown which give information of the relative compositions of Ni, Co and Se in the elemental mapping. The scale bars for both panels (Ni, Co and Se) are the same. (right) Compositional line profile for Ni, Co and Se recorded along the red line (from left to right) in the STEM images. (h) XRD pattern of u-NCSe. (i) Band structure and density of state calculations for the $NiCo_2Se_4$ phase.

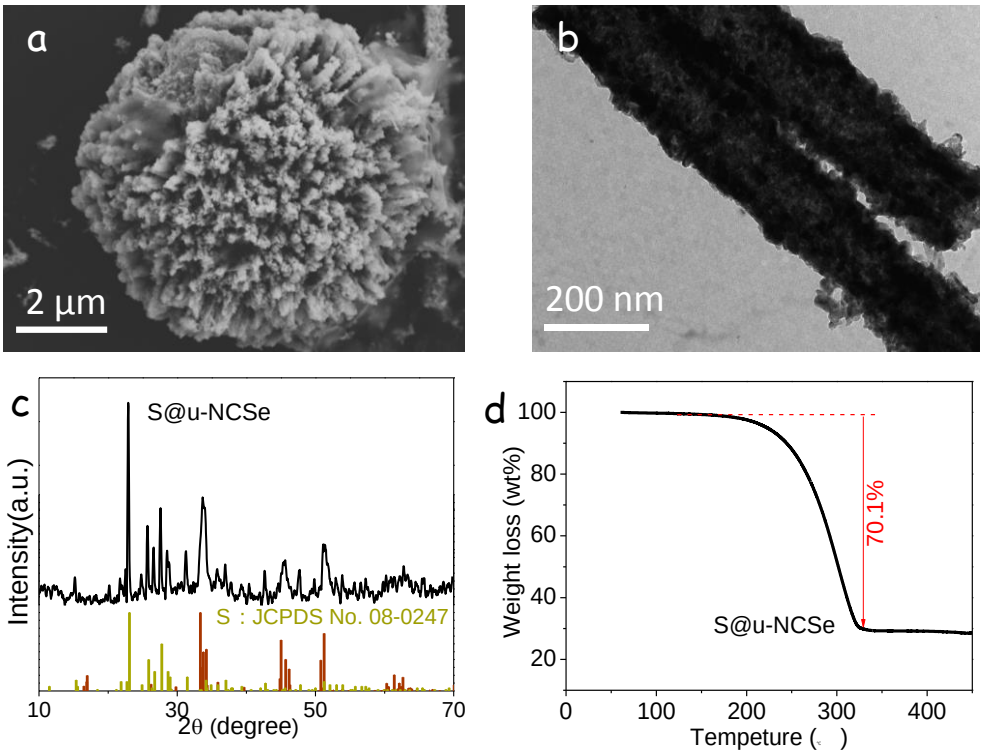

Figure 3. (a) SEM image and (b) TEM image of S@u-NCSe composite. (c) XRD pattern of S@u-NCSe. (d) TGA curve of S@u-NCSe composite measured in N_2, showing a large weight loss % during heating up, corresponding to a sulfur loading ratio of ~70.1 wt.%.

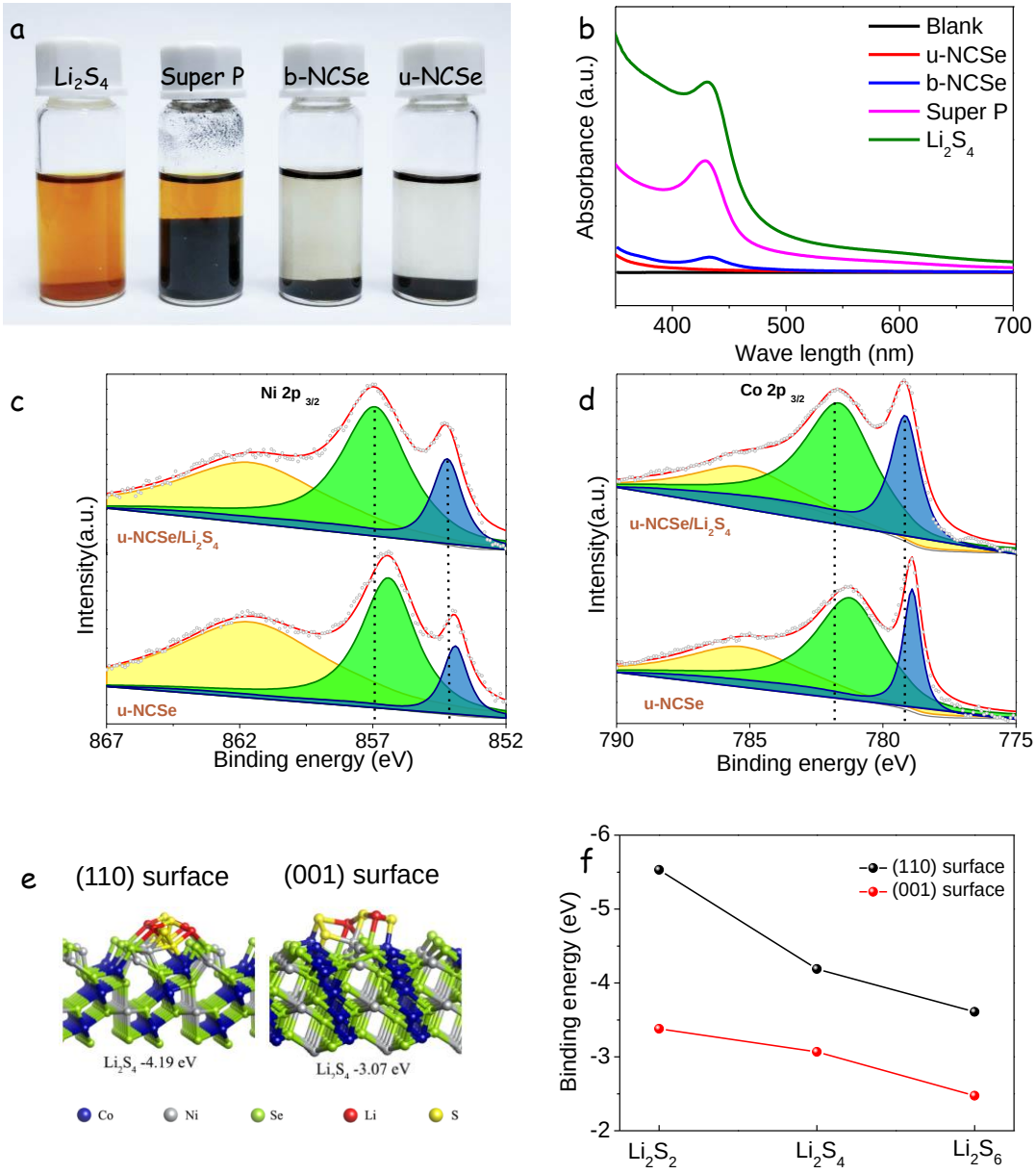

Figure 4. Strong static interaction between u-NCSe and LiPS. (a) Photograph and (b) UV−vis spectra of the polysulfide solution after exposure to the different adsorbers. (c, d) High-resolution XPS spectra of Ni 2p3/2 and Co 2p3/2 of u-NCSe before and after adsorption of Li_2S_4. (e) Relaxed Li_2S_4-adsorbed structures on both (110) (left) and (001) (right) surfaces of $NiCo_2Se_4$ calculated with DFT. (f) Calculated binding energy between LiPSs (Li_2S_2, Li_2S_4, and Li_2S_6) and $NiCo_2Se_4$ surfaces.

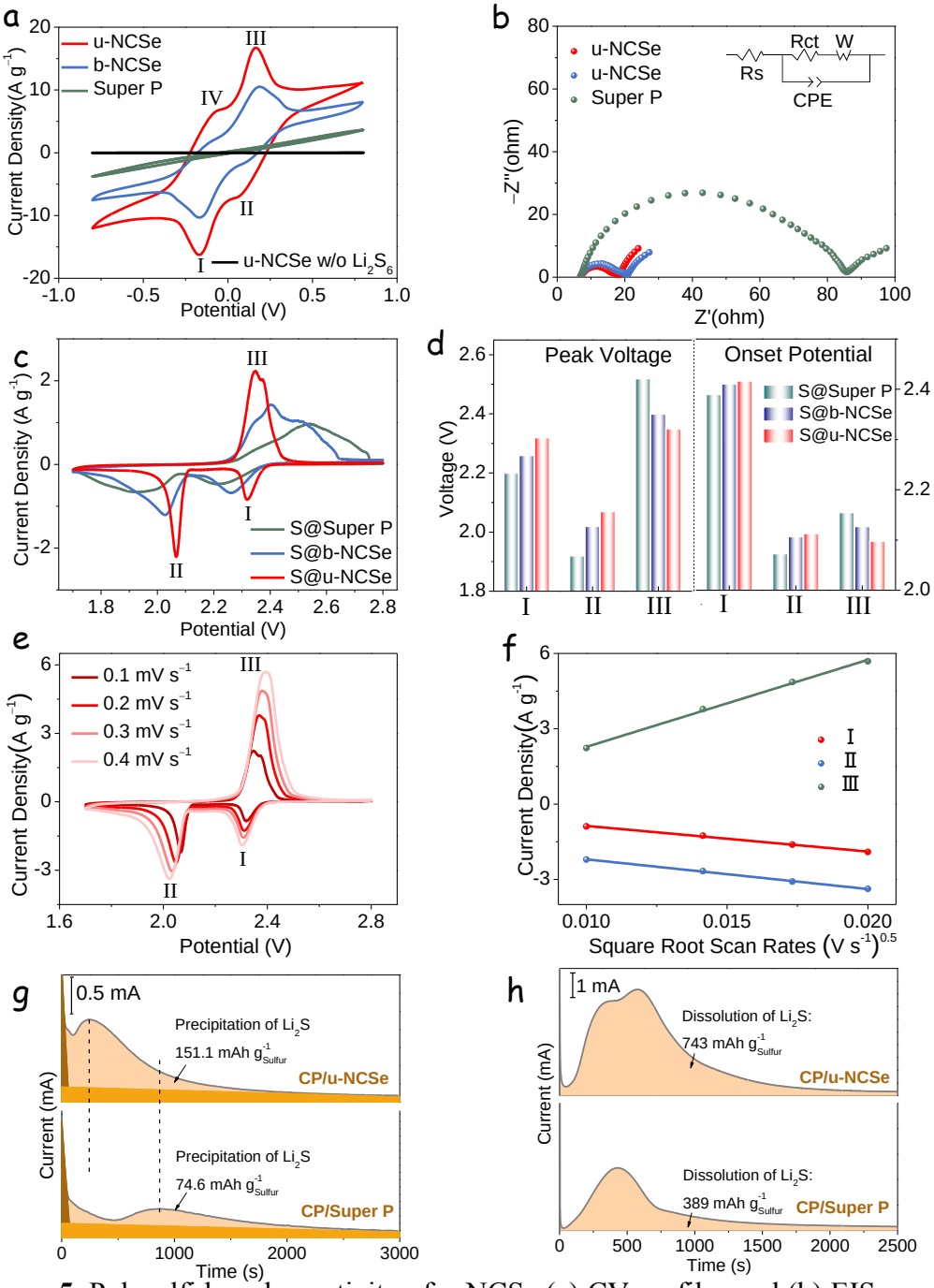

Figure 5. Polysulfide redox activity of u-NCSe (a) CV profiles and (b) EIS spectra of symmetrical cells with different host materials using an electrolyte containing 0.5 mol L^{-1} Li_2S_6 and 1 mol L^{-1} LiTFSI dissolved in DOL/DME (v/v = 1/1) . (c) CV profiles of Li-S cells with different electrodes. (d) Corresponding peak voltages and onset potentials of asymmetrical Li-S cells obtained from the CV curves. (e) CV curves of S@u-NCSe electrode at various scan rates. (f) Plot of CV peak current for peaks I, II , and III versus the square root of the scan rates. (g) Potentiostatic discharge profile at 2.05 V

on different electrodes with Li_2S_8 catholyte. (h) Potentiostatic charge profile at 2.40 V for evaluating dissolution kinetics of Li_2S.

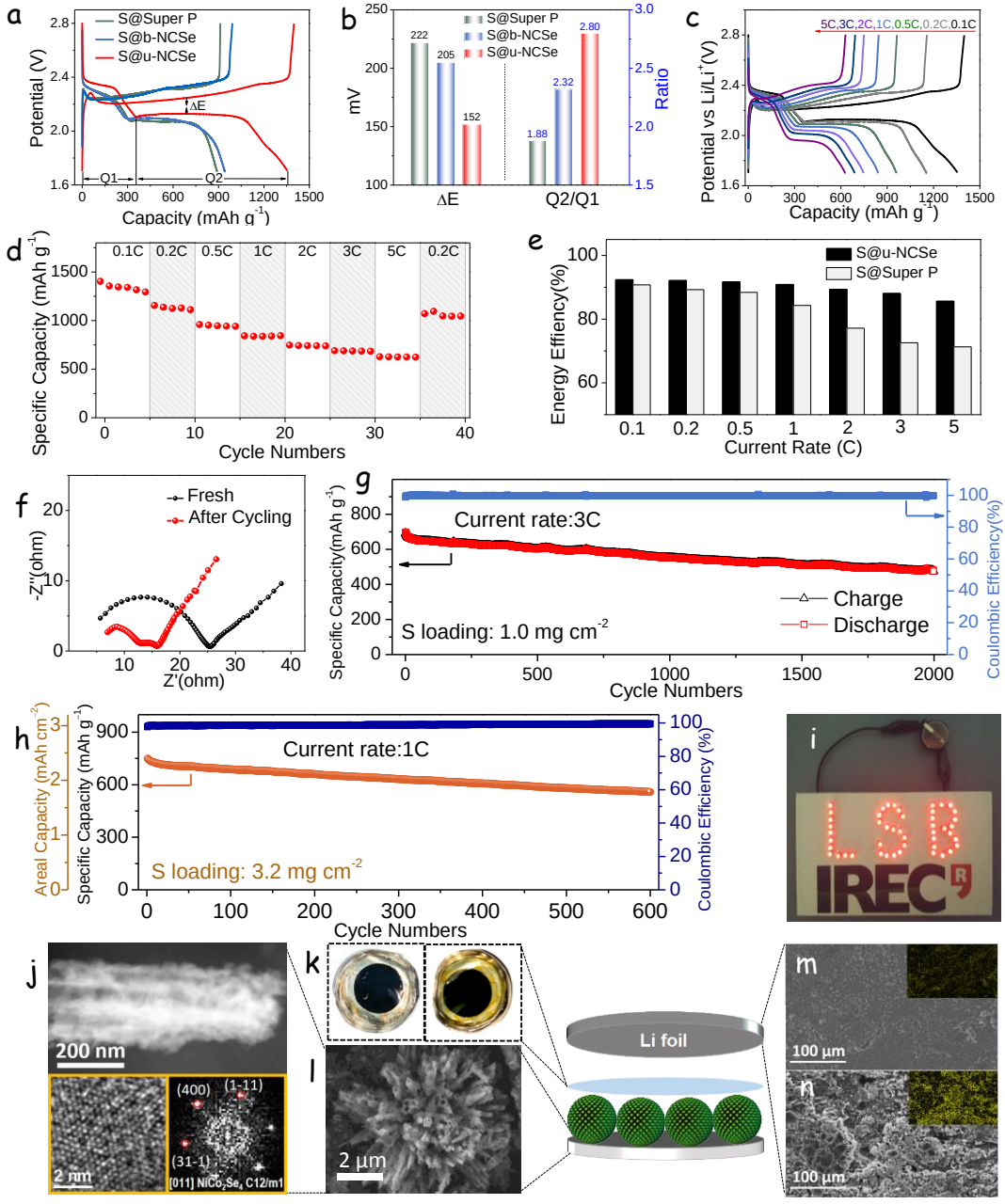

Figure 6. Electrochemical performance of coin cells (a) Charge/discharge curves of different electrodes at current rate of 0.1 C. (b) The value of Δ E an Q2/Q1 obtained from charge/discharge curves. (c, d) Charge/discharge curves and rate capability of the S@u-NCSe composite at various C rates from 0.1 C to 5 C. (e) Energy efficiency at different current densities. (f) EIS spectra of S@u-NCSe electrode before and after

100 cycles at 1 C. (g) capacity retention at 3 C. (h) Cycling performance of electrodes with a 3.2 mg cm^{-2} sulfur-loading. (i) Digital photographs of 47 red LED lamps powered by one S@u-NCSe Li-S coin cell. After cycling at 1 C for 200 cycles, (j) HAADF-STEM and HRTEM micrographs of S@u-NCSe and corresponding FFT spectrum. (k) Separators of coin cells with S@u-NCSe cathode (left) and S@Super P cathode (right), (l) SEM micrograph of S@u-NCSe electrode, and (m, n) surface of lithium foil from S@u-NCSe and S@Super P coin cells. Inset images in (m, n) are EDX mapping images showing sulfur signal.

The Table of Contents Entry

Rational designed u-NCSe as efficient sulfur hosts are synthesized to overcome the barriers of LSBs simultaneously. Benefited from a hollow structure to relieve volumetric expansion, superior electrical conductivity to improve electron transfer, high polarity to promote absorption of LiPS, and outstanding electrocatalytic activity to accelerate LiPS conversion kinetics, S@u-NCSe electrodes deliver long-life and high-rate electrochemical performance.

Keywords: nickel cobalt selenide, catalytic effect, polarity, hollow nanostructure, lithium sulfur batteries

C. Q. Zhang, J. J. Biendicho,* T. Zhang, R. F. Du, J. S. Li, X. H. Yang, J. Arbiol, Y. T. Zhou,* J. R. Morante, A. Cabot*

Combined High Catalytic Activity and Efficient Polar Tubular Nanostructure in Urchin-like Metallic $NiCo_2Se_4$ for High Performance Lithium Sulfur Batteries

ToC Figure